THE JOURNAL OF PHYSICAL CHEMISTRY C
A JOURNAL OF THE AMERICAN CHEMICAL SOCIETY

pubs.acs.org/JPCC

Article

# The $MoS_2$-Graphene-Sapphire Heterostructure: Influence of Substrate Properties on the $MoS_2$ Band Structure

Henrik Wördenweber, Annika Grundmann, Zhaodong Wang, Susanne Hoffmann-Eifert,* Holger Kalisch, Andrei Vescan, Michael Heuken, Rainer Waser, and Silvia Karthäuser*

Cite This: *J. Phys. Chem. C* 2023, 127, 10878−10887

Read Online

ACCESS | Metrics & More | Article Recommendations | Supporting Information



**ABSTRACT:** Van der Waals $MoS_2$/graphene heterostructures are promising candidates for advanced electronics and optoelectronics beyond graphene. Herein, scanning probe methods and Raman spectroscopy were applied for analysis of the electronic and structural properties of monolayer (ML) and bilayer 2H-$MoS_2$ deposited on single-layer graphene (SLG)-coated sapphire (S) substrates by means of an industrially scalable metal organic chemical vapor deposition process. The SLG/S substrate shows two regions with distinctly different morphology and varied interfacial coupling between SLG and S. ML $MoS_2$ nanosheets grown on the almost free-standing graphene show no detectable interface coupling to the substrate, and a value of 2.23 eV for the $MoS_2$ quasiparticle bandgap is determined. However, if the graphene is involved in hydrogen bonds to the hydroxylated sapphire surface, an increased $MoS_2$/graphene interlayer coupling results, marked by a shift of the conduction band edge toward Fermi energy and a reduction of the ML $MoS_2$ quasiparticle bandgap to 1.98 eV. The surface topography reveals a buckle structure of ML $MoS_2$ in conformity with SLG that is used to determine the dependence of the ML $MoS_2$ bandgap on the interfacial spacing of this heterostructure. In addition, an in-gap acceptor state about 0.9 eV above the valence band minimum of $MoS_2$ has been observed on locally elevated positions on both SLG/S regions, which is attributed to local bending strain in the grown $MoS_2$ nanosheets. These fundamental insights reveal the impact of the underlying substrate on the topography and the band alignment of the ML $MoS_2$/SLG heterostructure and provide the possibility for engineering the quasiparticle bandgap of ML $MoS_2$/SLG grown on controlled substrates that may impact the performance of electronic and optoelectronic devices therewith.

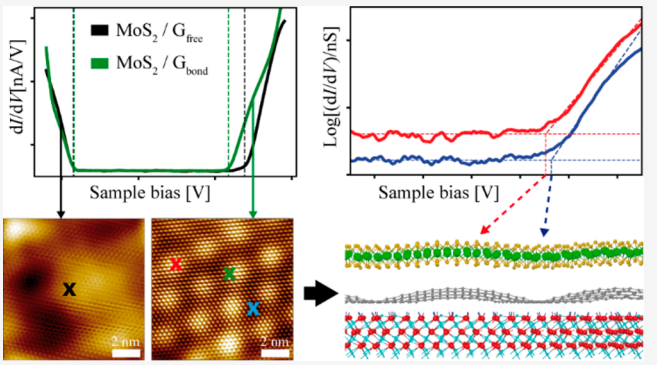


## 1. INTRODUCTION

Semiconducting molybdenum disulfide ($MoS_2$) is a prominent representative of transition-metal dichalcogenides (TMDCs) that forms layered two-dimensional (2D) materials with strong covalent bonds between metal and chalcogen atoms in the layer and weak van der Waals (vdW) interactions between the layers.[1,2] TMDCs exhibit an intrinsic bandgap partly within the visible spectrum,[3,4] which can be tuned by the number of layers[5,6] or the dielectric properties of the environment,[7] and a large exciton binding energy allowing for charged excitons.[3,4,8] By combining different TMDCs or TMDCs with other conducting or insulating 2D materials, like for example graphene[9] and hexagonal boron nitride,[10] heterostructures suitable for nanoelectronic and optoelectronic devices can be compiled.[11−13]

Especially heterostructures consisting of the photoresponsive $MoS_2$ and the semimetallic graphene, exhibiting a high carrier mobility, turn out to be an advantageous combination for device applications.[14−16] Employing the $MoS_2$/graphene heterostructure allows to fabricate, for example, large-scale 2D field effect transistors, with $MoS_2$ as channel material and graphene as contacts, or rewritable optoelectronic switches.[15,16] Prerequisites for practical applications of the $MoS_2$/graphene heterostructure are high-quality $MoS_2$ crystals, wafer-scale processability, and large-area uniformity. Recently, due to the technical progress in deposition methodology, the commensurate growth of $MoS_2$ on graphene was demonstrated by different groups using chemical vapor deposition (CVD),[17] molecular beam epitaxy,[18] atomic layer deposition,[19] and metal−organic vapor phase epitaxy (MOVPE).[20−22] These high-quality thin films grown by vdW epitaxy on technically relevant substrates show nearly strain-free $MoS_2$ in registry with graphene.[17] Furthermore, monolayer (ML) $MoS_2$/

Received: April 14, 2023
Revised: May 9, 2023
Published: May 30, 2023

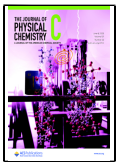

graphene heterostructures are strongly influenced by the roughness of the supporting substrate, since graphene exhibits a high conformity to substrates.[23] Therefore, reducing the surface roughness of the supporting substrate is essential to ensure large-area uniformity of the $MoS_2$−graphene interface and to meet the demands of lithography in device fabrication.

It is well-known that the bandgap of ML $MoS_2$ depends strongly on charge states, biaxial strain, as well as on the dielectric properties of the respective substrate and its interaction strength with $MoS_2$.[1,7,24−26] However, even if a distinct substrate is chosen and only charge neutral, strain-free $MoS_2$ MLs are considered, largely varying quasiparticle energy gaps are reported. Like this, the experimentally obtained bandgaps reported for ML $MoS_2$/graphene vdW heterostructures with seemingly constant interface coupling range from 2.0 to 2.55 eV.[17,18,25,27,28] This large range of reported quasiparticle bandgaps for ML $MoS_2$ on graphene can be explained only in part by theoretical studies, which predict possible bandgap variations caused by the modification of the interlayer spacing and by variations of the interlayer orientation of $MoS_2$ with respect to graphene.[29−31] Hence, no conclusive evidence to explain the widespread experimentally obtained quasiparticle bandgaps of the ML $MoS_2$/graphene heterostructure is available, and further investigations are needed.

Here, we use as substrate high-quality single-layer graphene (SLG) grown in a first CVD step on wafer-scale $H_2$-etched c-plane sapphire ($\alpha$-$Al_2O_3$ (0001)). It has been inspected in-depth by scanning tunneling microscopy (STM) and spectroscopy (STS) methods as described very recently.[32] We found that CVD grown SLG on $H_2$-etched sapphire (S) exhibits local variations in the SLG/S interface, emerging as almost free-standing SLG near sapphire step edges ($G_{free}$) and weakly bonded SLG on sapphire terraces ($G_{bond}$), respectively.[32] Using this SLG/S heterostructure as a substrate, ML and bilayer (BL) $MoS_2$ nanosheets were deposited applying the recently developed MOVPE process.[22] In the current study, we pay special attention to the electronic properties of the $MoS_2$/SLG/S heterostructure, like bandgap, band alignment, and in-gap states. In this connection, we focus especially on the influence of local variations, that is, the specific topography and the different electronic properties of the two substrate regions, $G_{free}$/S and $G_{bond}$/S. The results are gained with well-established STM and STS methods revealing electronic properties at well-defined positions on the 2D material surface.[12,32−35] These insights are additionally supported by scanning electron microscopy (SEM), Raman spectroscopy, and atomic force microscopy (AFM).

## 2. EXPERIMENTAL SECTION

**2.1. Deposition Process.** A time-tested process was used to deposit a closed film of SLG on a 2″ $\alpha$-$Al_2O_3$ (0001) wafer with a nominal offcut of 0.2° toward the m-plane in a commercial AIXTRON cold-wall close-coupled showerhead (CCS) reactor in 6 × 2″ geometry. A thermal pretreatment of the wafer was performed at 1400 °C under $H_2$ at 150 mbar for several minutes. Thereafter, SLG was deposited at 1400 °C and 500 mbar for 160 s in a mixture of argon and $CH_4/H_2$ in a flow ratio of 1/13.3. In a second step, $MoS_2$ was grown in an AIXTRON planetary hot-wall reactor in 10 × 2″ configuration at 750 °C and 30 hPa resulting in a noncoalesced film consisting of ML and BL nanosheets. Molybdenum hexacarbonyl (MCO, purity 99.9%) and di-*tert*-butyl sulfide (DTBS, purity 99.999%), both Dockweiler Chemicals, served as precursors, and $N_2$ served as carrier gas. The MCO and DTBS molar flows were set to 20 nmol/min and 19 $\mu$mol/min, respectively.[22] The $MoS_2$ growth process was optimized in a series using different $MoS_2$ deposition times. To obtain a submonolayer coverage, the $MoS_2$ growth process was intentionally set to 1 h. The samples were stored in argon, and exposure to atmosphere was limited to minutes, which allows a long-time storage over a month without degradation.

**2.2. Surface Analysis and Optical Spectroscopy.** SEM measurements were performed using a commercial Hitachi SU8000 electron microscope operating at room temperature and a chamber pressure of $10^{-7}$ mbar. The SLG was grounded during the measurements, and an acceleration voltage of 0.7 kV was applied.

Raman spectroscopy was conducted using a room temperature confocal Raman microscope (XploRa Plus, HORIBA France SAS) equipped with a 532 nm solid-state laser. The laser power was adjusted to 8 mW, and the beam was focused via a 100× microscope objective lens to a spot size of ca. 0.5 $\mu$m in diameter. The $MoS_2$ phonon active region from 200 to 900 $cm^{-1}$ was recorded in 30 × 30 mapping measurements with a step size of 0.4 $\mu$m, a 1800 $mm^{-1}$ grating, an exposure time of 8 s, and five accumulations. The graphene region from 1300 to 2900 $cm^{-1}$ was recorded in 20 × 20 mapping measurements with a step size of 0.5 $\mu$m, a 1200 $mm^{-1}$ grating, an exposure time of 8 s, and five accumulations. The measurements were recorded using LabSpec 6 spectroscopic suite software from HORIBA. Analysis of the spectra including baseline subtraction and Lorentzian peak fitting was applied to all individual spectra of the mapping measurements mentioned above using Python (cf. Supporting Information, Figure S1). The resulting values for the peak positions of $MoS_2$ ($E^1_{2g}$ and $A_{1g}$) and SLG (G and 2D) as well as the corresponding intensity ratios were plotted in histograms, which were fitted with Gaussian shapes (Supporting Information, Figure S1).

A commercial Cypher AFM (Asylum Research) with AFM probes from Nanosensors was used for the AFM measurements. The AFM images were recorded using the tapping mode and analyzed utilizing the Mountain SPIP analytical software.

**2.3. STM and STS Analysis.** The STM and STS measurements were performed in a commercial low-temperature STM from CreaTec Fischer. The STM chamber operates in ultrahigh vacuum below $10^{-10}$ mbar, at a temperature of 4.2 K, and with custom-made electrochemically etched tungsten tips. The measurement parameters are given for each image in the caption. The STM images were plane corrected and optionally noise filtered using Mountain SPIP analytical software. The shown STS measurements were done utilizing an internal lock-in amplifier operating at 973 Hz. A correction of the DC offset of the lock-in amplifier, visible in the $dI/dV$ data, was performed by simultaneously recording the full $I/V$ curves and taking the numerical derivative. The STS curves were slightly smoothed, plotted, and analyzed with Python.

## 3. RESULTS AND DISCUSSION

In this study, we use as substrate the thoroughly characterized heterostructure SLG on wafer-scale, $H_2$-etched $\alpha$-$Al_2O_3$ (0001).[32] Thereon, $MoS_2$ nanosheets were deposited applying vdW epitaxy (MOVPE).[22] SEM imaging was used for a first large-scale analysis of the resulting 2D heterostructure $MoS_2$/SLG/S (Figure 1). The deposition of $MoS_2$ with a coverage of


https://doi.org/10.1021/acs.jpcc.3c02503
J. Phys. Chem. C 2023, 127, 10878−10887

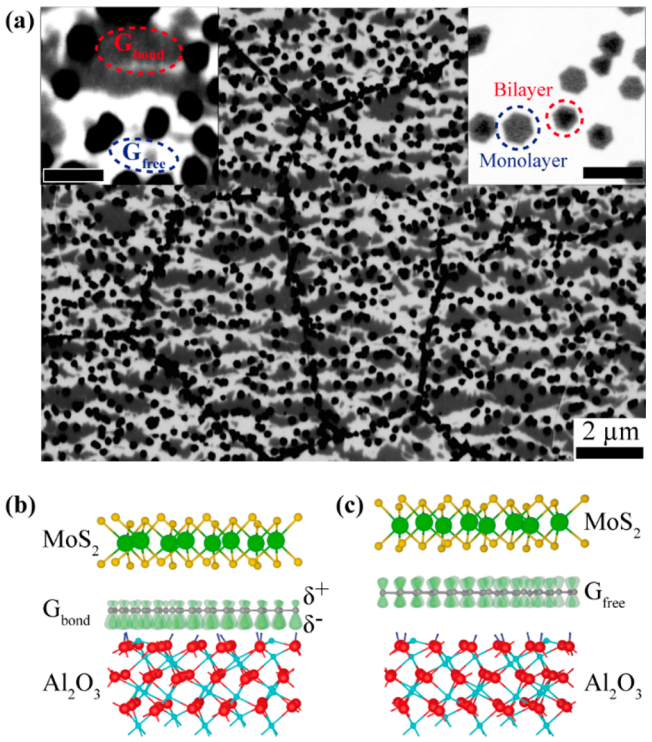


**Figure 1.** (a) SEM image of the $MoS_2$/SLG/S heterostructure with the $MoS_2$ nanosheets appearing in black. Left inset: magnification of $MoS_2$ nanosheets deposited on $G_{bond}$ and $G_{free}$. Right inset: contrast setting was adjusted so that ML and BL $MoS_2$ nanosheets can be distinguished (scale bars in both insets: 0.4 $\mu$m). The SEM images shown in the insets were recorded with higher resolution in the region next to the main image. Schematics showing the vertical stacking of the heterostructures in different surface regions with (b) graphene weakly coupled to sapphire, $MoS_2/G_{bond}/S$, and (c) free-standing graphene, $MoS_2/G_{free}/S$. Color code: O (red), Al (cyan), H (blue), C (gray), S (yellow), Mo (lime-green), and SLG $\pi$-orbitals (dark-green).

20.7 ± 1.7% results in uniform hexagonal crystals with an average diameter of 200 ± 10 nm evenly distributed throughout the SLG surface. There is no preference of adsorption to darker or brighter appearing surface areas of the SLG/S substrate but a small nucleation preference at high step edges, visible as black lines in Figure 1a. The darker and brighter regions on the substrate, see also the left inset of Figure 1, are due to variations in the coupling between SLG and $H_2$-etched sapphire. Details are described in our recent study.[32] The reduced SLG/S interlayer coupling, predominantly provoked by sapphire step edges, leads to nearly free-standing, highly conducting SLG regions (Figure 1c), while weakly bonded SLG regions (Figure 1b) are observed on sapphire terraces. The latter exhibit a reduced conductivity by a factor of 4, discernible by the different contrast in SEM images.[32] The nucleation and growth of $MoS_2$ nanosheets take place similarly on both substrate regions, $G_{free}$ and on $G_{bond}$. In addition to ML nanosheets (17.5 ± 1.5% of the total substrate area), BL (3.2 ± 1.0%) and in very rare cases trilayer nanosheets (<0.2 ± 0.2%) can be observed, all with hexagonal shape (Figure 1a, right inset).

The vertical stacking of the heterostructures $MoS_2/G_{bond}/S$ and $MoS_2/G_{free}/S$ is displayed in Figure 1b,c, respectively, to illustrate the inherent differences in interlayer spacing of $G_{bond}$ and $G_{free}$ to the $H_2$-etched sapphire substrate. $G_{bond}$ and $G_{free}$ are located at minimum distances of 0.26 and 0.38 nm to $\alpha$-$Al_2O_3$ (0001), respectively, as deduced in ref 32. Since the distance of 0.38 nm is considerably larger than the graphite interlayer distance (0.334 nm), only minor vdW interactions between $G_{free}$ and the supporting sapphire can be expected. On the other hand, $G_{bond}$ exhibits a considerable interface coupling with sapphire as verified by the formation of a moiré superstructure (with a period of 2.66 nm), a bandgap opening of graphene (about 73 meV), and the decreased conductivity (factor 4) compared to $G_{free}$.[32] The size of the $MoS_2$ − SLG vdW gap (0.34 nm) and the $MoS_2$ ML thickness (0.32 nm) in the schematics (Figure 1b,c) are adopted from the literature.[12,29−31]

Large-area Raman mapping measurements were performed on the $MoS_2$/SLG/S heterostructure and an SLG/S reference sample. Exemplary Raman spectra are given in Figure 2a exhibiting the most prominent peaks of graphene, $\alpha$-$Al_2O_3$ (0001), and $MoS_2$, while the mean values for the characteristic graphene (G, 2D) and $MoS_2$ ($E^1_{2g}$ and $A_{1g}$) frequencies are listed together with the averaged intensity ratios 2D/G and D/G in Table 1. The positions of the $MoS_2$ Raman peaks $E^1_{2g}$ and $A_{1g}$ depend on multiple factors, like the number of layers, strain effects, the twist angle between $MoS_2$ and graphene, as well as doping.[36−39] Consequently, a disentanglement of all different effects from only Raman measurements is not possible.[40] However, the separation between the $MoS_2$ $E^1_{2g}$ and $A_{1g}$ peaks

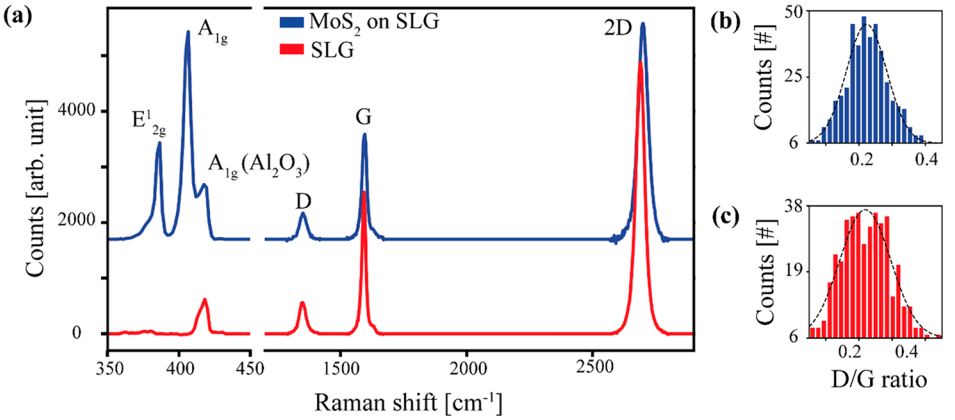


**Figure 2.** (a) Raman spectra of $MoS_2$ deposited on SLG/S (blue) and a reference sample SLG/S (red). (b,c) Histograms of the D/G intensity ratio of graphene in $MoS_2$/SLG/S and SLG/S resulting from a 10 × 10 $\mu$m Raman map, with 20 × 20 data points.



https://doi.org/10.1021/acs.jpcc.3c02503
J. Phys. Chem. C 2023, 127, 10878−10887

Table 1. Raman Peak Positions of $MoS_2$ ($\Delta\omega(E^1_{2g})$ and $\Delta\omega(A_{1g})$) and SLG ($\Delta\omega(G)$ and $\Delta\omega(2D)$) as well as Corresponding Intensity Ratios ($I_{2D}/I_G$, $I_D/I_G$)[a]

| | $MoS_2$ | | | |
|---|---|---|---|---|
| | $\Delta\omega(E^1_{2g})/cm^{-1}$ | | $\Delta\omega(A_{1g})/cm^{-1}$ | |
| $MoS_2$/SLG/S (this work) | 385.9 ± 0.3 | | 406.4 ± 0.6 | |
| $MoS_2$/FLG[40] | 385.0 | | 404.9 | |
| $MoS_2$/SLG/$SiO_2$[36] | 384.9 | | 404.4 | |
| | Graphene | | | |
| | $\Delta\omega(G)/cm^{-1}$ | $\Delta\omega(2D)/cm^{-1}$ | $I(2D)/I(G)$ | $I(D)/I(G)$ |
| $MoS_2$/SLG/S (this work) | 1590.9 ± 1.6 | 2691.2 ± 3.2 | 2.35 ± 0.17 | 0.22 ± 0.06 |
| SLG/S (this work) | 1590.0 ± 2.1 | 2684.1 ± 2.7 | 2.15 ± 0.24 | 0.22 ± 0.08 |
| Supported, charge neutral, strain-free SLG[43−45] (see text) | 1582 | 2676 | | |

[a]The mean peak positions were taken from Gaussian fits of histograms resulting from Raman mappings (Supporting Information, Figure S1).

can be correlated to the number of deposited $MoS_2$ layers. While $MoS_2$ monolayers sandwiched between two polymer layers exhibit an $E^1_{2g}$ to $A_{1g}$ distance of 18−20 $cm^{-1}$, the frequency difference of BL $MoS_2$ on the same substrate amounts to 22 $cm^{-1}$, and a value of 25 $cm^{-1}$ is given for bulk $MoS_2$.[41] However, an ML $MoS_2$ on graphene exhibits a frequency difference of up to 21 $cm^{-1}$.[42] For the sample under investigation, we find a bimodal distribution of the $MoS_2$ $E^1_{2g}$ peaks from the mapping measurements with the main peak at 385.9 ± 0.2 $cm^{-1}$ and a side peak at 385.2 ± 0.6 $cm^{-1}$. The averaged peak position of the $A_{1g}$ peaks was obtained at 406.4 ± 0.6 $cm^{-1}$ (Supporting Information, Figure S1k,l). Accordingly, the measured Raman signals with frequency differences of 20.5 ± 0.6 $cm^{-1}$ (between the main $E^1_{2g}$ peak and $A_{1g}$) and 21.2 ± 0.8 $cm^{-1}$ (between the $E^1_{2g}$ side peak and $A_{1g}$) indicate the dominance of ML $MoS_2$, while BL $MoS_2$ is present to a minor amount. This is highly consistent with the above extracted surface coverages from SEM measurements.

The values for the $MoS_2$ $E^1_{2g}$ and $A_{1g}$ peak positions are both slightly blue-shifted with respect to values around 385 and 405 $cm^{-1}$, respectively, that have been determined for relaxed ML $MoS_2$ on a few layers of graphene (FLG) or transferred ML $MoS_2$ on various substrates.[40] According to the literature, the observed blue-shift corresponds to a compressive strain of about 0.43% assuming uniaxial strain, while it would amount to less than 0.2% if biaxial strain is considered.[17,37,41] Thus, our $MoS_2$ Raman signals can be explained overall by the dominating presence of ML $MoS_2$ and minor compressive strain, which is probably due to the difference in lattice constants between $MoS_2$ and graphene. It should be noted that we observe a considerably smaller blue-shift of the $A_{1g}$ peak than recently reported for ML $MoS_2$ deposited on epitaxial graphene on SiC ($A_{1g}$ at 407.2 $cm^{-1}$) or on a differently processed SLG/S substrate ($A_{1g}$ at 407.3 $cm^{-1}$).[17,18] A large blue-shift of the $A_{1g}$ peak is usually interpreted as hole doping, which obviously plays a minor role in our case.[17,18,39]

The mean values of the graphene specific peaks (G and 2D) as well as the 2D/G and D/G intensity ratios of the reference SLG/S heterostructure agree well with the corresponding values reported previously.[32] The ratio 2D/G larger than 2 and D/G = 0.22 (Figure 2c) indicate single-layer graphene with a low defect density prior to the deposition of the $MoS_2$ layer. The G and 2D peaks at 1590.0 ± 2.1 and 2684.1 ± 2.7 $cm^{-1}$ are both blue-shifted compared to mean peak positions for charge neutral, strain-free graphene with a similar interlayer coupling (for details see Supporting Information, Figure S2).[43−45] Applying the procedure of Lee et al. to separate the mechanical strain effect and the charge doping effect on the Raman frequencies G and 2D, we find a minor compressive strain of about 0.1% and a small charge concentration below $10^{13}$ $cm^{-2}$ for SLG on $H_2$-etched $\alpha$-$Al_2O_3$ (0001).[46] The slight compressive strain on SLG is due to the cool down from deposition temperature, and the p-doping results from the interlayer interaction with the sapphire substrate, as shown previously.[32,47]

After the deposition of $MoS_2$ on the SLG/S heterostructure, we find the intensity ratios 2D/G and D/G (Figure 2b, Table 1) almost unchanged, pointing to a smooth deposition process without the generation of additional defects in the SLG. While the G peak position is almost unchanged, the 2D peak position obtained from the $MoS_2$/SLG/S heterostructure is further blue-shifted (7.1 $cm^{-1}$) compared to SLG/S. A major part of this 2D peak shift is caused by an increased interlayer coupling of SLG sandwiched between $MoS_2$ and sapphire.[36] Yang et al. did observe the same shift of merely the 2D peak after deposition of $MoS_2$ on top of SLG.[48] It is attributed to an interlayer coupling effect due to an increased dielectric screening and the modified out-of-plane vibrations of SLG embedded into a heterostructure.[36,49] The compressive strain and the p-doping, both observed in the SLG/S substrate as well, are supposed to remain almost constant after $MoS_2$ deposition (Supporting Information, Figure S2).

The $MoS_2$ nanosheets were further investigated by high-resolution STM and STS to determine the impact of the distinct SLG/S substrate regions, $G_{bond}$/S and $G_{free}$/S, characterized by different topographic and electronic properties, on the band alignment of $MoS_2$. In Figure 3, an ML $MoS_2$ nanosheet with a clear hexagonal shape partially covered by a second layer is shown. The transition between the two SLG regions, $G_{bond}$ and $G_{free}$, of the underlying substrate is indicated by the white dashed line in the image. A thorough step height analysis of the features presented in the image is given in Supporting Information, Figure S3, together with a comparison to AFM heights. The determined apparent step heights of the first and second $MoS_2$ layer amount to 0.90 ± 0.02 nm and 0.63 ± 0.02 nm ($V_{bias}$ = 2.3 V), respectively, and are in line with previously reported $MoS_2$ values for these conditions.[17] AFM measurements confirm a slight difference in step heights between the first (0.73 ± 0.05 nm) and the following $MoS_2$ layer step (0.67 ± 0.05 nm). Both values conform with earlier reports of the $MoS_2$ ML thickness determined from AFM experiments (0.70 nm) and scanning high-resolution transmission electron microscopy cross sections (0.65 nm) as well as theoretical studies (0.66 nm).[17,29,31,50]



https://doi.org/10.1021/acs.jpcc.3c02503
J. Phys. Chem. C 2023, 127, 10878−10887

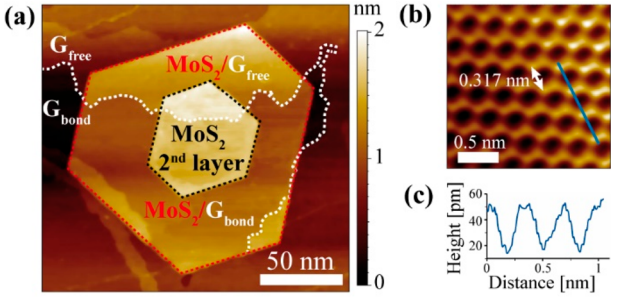


**Figure 3.** STM of the $MoS_2$/SLG/S heterostructure. (a) Single $MoS_2$ nanosheet grown over the two SLG areas, $G_{bond}$ and $G_{free}$, indicated by a dotted white line to enhance the visibility ($I_{set}$ = 0.29 nA and $V_{bias}$ = 2.3 V). (b) Atomic-scale image of ML $MoS_2$ on delaminated SLG ($G_{free}$). The lattice constant of $MoS_2$, 0.317 nm, and a cross section are marked (blue, $I_{set}$ = 0.59 nA and $V_{bias}$ = 1 V). (c) Apparent height along the cross section indicated in (b).

High-resolution images of ML $MoS_2$ deposited on both SLG regions, $G_{bond}$ and $G_{free}$, exhibit no observable difference in the atomic surface structure. An exemplary STM measurement representing the top sulfur layer of $MoS_2/G_{free}$ is shown in Figure 3b exhibiting an S···S atomic distance of 0.317 ± 0.002 nm in good agreement with experimental values and crystal structure data (0.316 nm).[17,51−53] This finding is consistent with the Raman measurements showing that $MoS_2$ is not significantly strained. A comparison of the crystallographic orientation of $MoS_2$ and SLG indicates a twist angle of around 2 ± 2° (Supporting Information, Figure S4), suggesting that either no or only a very low twist angle is present. Furthermore, a parallel orientation of the crystallographic directions of $MoS_2$ and SLG points to the formation of the most stable commensurate $MoS_2$/SLG heterostructure (hexagonal structure, 2H) with a supercell constructed by 4 × 4 $MoS_2$ cells matching 5 × 5 graphene cells. The optimal supercell is reached by a compression of the $MoS_2$ layer of only 0.3%,[29,30] all consistent with our findings. Here, we can exclude the presence of 1T-$MoS_2$, which is a metastable, metallic structure that shows a significant catalytic activity (Supporting Information, Figures S1 and S4). Furthermore, 1T-$MoS_2$ would be unambiguously identified by its electronic states using STS. It should be noted that no atomic defects are observed, which are expected to be easily accessible in STM images of $MoS_2$ layers.[52,54,55] Therefore, we conclude that the here deposited $MoS_2$ nanosheets are nearly defect free due to the chosen MOVPE deposition process.

Insights into the band structure of the $MoS_2$/SLG/S stacking were gained by STS measurements on multiple-ML and -BL $MoS_2$ nanosheets grown on $G_{bond}$ and $G_{free}$ (Figure 4). The valence band maximum (VBM) and the conduction band minimum (CBM) were determined from curves of the logarithm of the differential conductance ($\log[(dI/dV)/nS]$) versus the bias voltage by fitting lines to the flanks of the curves on both sides.[34,35,56] The resulting quasiparticle bandgap (CBM − VBM) is larger for ML than for BL $MoS_2$ in accordance with the literature.[17] To rule out artifacts, like tip induced band bending, STS measurements were performed with decreasing tip−surface distance on different $MoS_2$ nanosheets (Figure 4b). Lowering the tip from the largest tip−surface distance, still allowing for stable measurements (at about 6 Å) by roughly 1 Å, no variations in the VBM or CBM are observed. Consequently, the bandgaps extracted from Figure 4b for ML $MoS_2/G_{free}/S$ (2.23 ± 0.06 eV) and ML $MoS_2/G_{bond}/S$ (1.98 ± 0.06 eV) mark distinct intrinsic interlayer properties.

Regarding the BL $MoS_2$ bandgap (Figure 4a) we find that for both BL $MoS_2$ grown on $G_{free}$ and $G_{bond}$, the CBM is measured at about 0.10 ± 0.04 eV, demonstrating that the influence of the SLG/S interface practically vanishes on the second $MoS_2$ layer (Figure 4a). Compared to ML $MoS_2$, the VBM of the BL is shifted to −1.50 ± 0.05 eV leading to a reduced bandgap of only 1.60 eV (exactly, 1.62 ± 0.05 eV and 1.58 ± 0.05 eV for BL $MoS_2/G_{free}/S$ and BL $MoS_2/G_{bond}/S$, respectively), which is in line with measurements of BL $MoS_2$ deposited on graphene/SiC and theoretical evaluations.[5,17]

Looking at the ML $MoS_2$/SLG/S heterostructure in more detail, we find the apparent CBM of $MoS_2/G_{free}$ at 0.40 ± 0.05 eV and the one of $MoS_2/G_{bond}$ at 0.16 ± 0.05 eV, while in both cases, the VBM is located at −1.83 ± 0.02 eV (Figure 4). Thus, the stronger binding of SLG to sapphire ($G_{bond}$ compared to $G_{free}$), which is an SLG/S interface property, shifts the CBM of ML $MoS_2$ to lower values and reduces the bandgap. This implies an enhanced interface coupling of ML $MoS_2$ to $G_{bond}/S$ compared to $G_{free}/S$.[31] Since the distance between $G_{free}$ and sapphire amounts to a minimal 0.38 nm (Figure 1c), $MoS_2$/

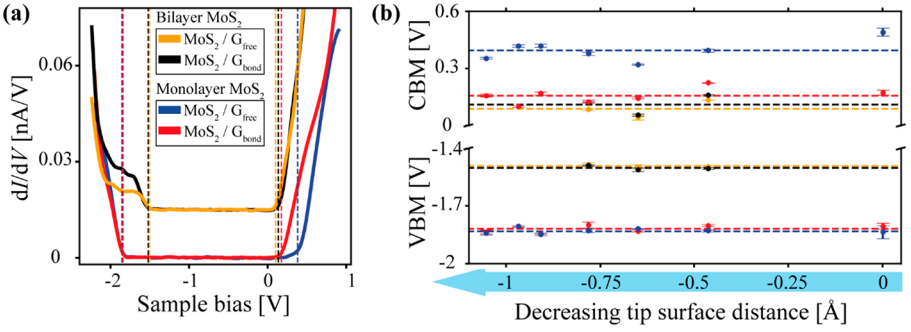


**Figure 4.** STS measurements on $MoS_2$ nanosheets deposited on $G_{bond}$ and $G_{free}$ ($I_{set}$ = 0.62 nA and $V_{stab}$ = 2 V). (a) Exemplary STS curves on ML and BL $MoS_2$ on both SLG regions with the respective VBM and CBM marked by dotted vertical lines. Plotted are slightly smoothed raw data with the curves corresponding to BL $MoS_2$ shifted upward by 0.015 nA/V. The DC offset of the lock-in amplifier was corrected for each measurement individually. (b) VBM and CBM for ML and BL $MoS_2$ nanosheets on $G_{bond}$ and $G_{free}$ as a function of the tip−surface distance, starting at $I_{set}$ = 0.15 nA and $V_{stab}$ = 2.0 V corresponding to 0 Å. The reduced tip−surface distances were adjusted by different stabilization voltages ($V_{stab}$ = 3.0 V to $V_{stab}$ = 0.7 V) at a constant current ($I_{set}$ = 0.62 nA). Each point in the diagram is the mean value out of 5 to 10 measurement points. Color code like in (a).



https://doi.org/10.1021/acs.jpcc.3c02503
J. Phys. Chem. C 2023, 127, 10878−10887

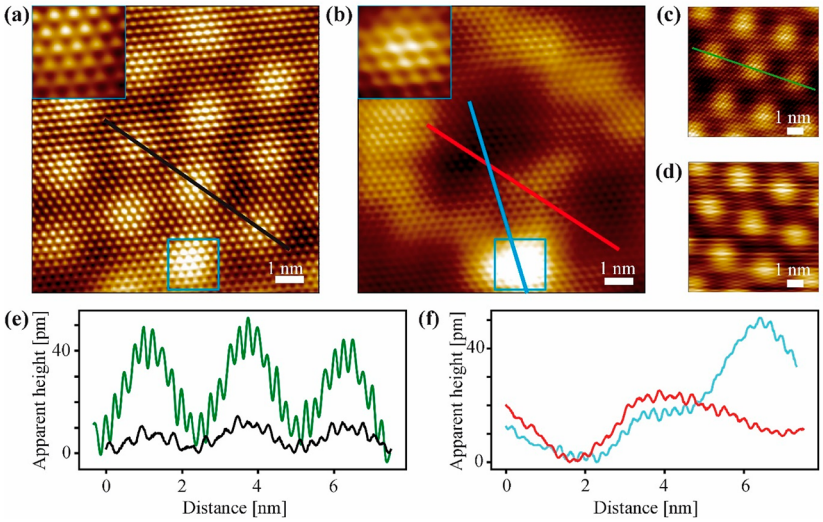


**Figure 5.** STM images on the identical position on $MoS_2/G_{bond}/S$ recorded (a) with a bias outside the bandgap ($I_{set}$ = 0.55 nA, $V_{bias}$ = −2.2 V) and (b) in the $MoS_2$ bandgap ($I_{set}$ = 0.55 nA, $V_{bias}$ = −1.2 V); the insets in (a) and (b) show zoom-in images of the 1.5 × 1.5 nm areas marked by blue squares. (c) STM on $G_{bond}/S$ ($I_{set}$ = 0.46 nA, $V_{bias}$ = −2.3 V); (d) STM on $G_{bond}/S$ ($I_{set}$ = 0.46 nA, $V_{bias}$ = −0.9 V). (e) Apparent height profiles of the $MoS_2$ buckle structure and the reference buckle structure of $G_{bond}/S$ along the black and the green lines in (a) and (c), respectively. (f) Cross section along the blue and the red lines marked in (b) with the red line being at the identical position as the black one in (a).

$G_{free}$ can be regarded as a free-standing heterostructure at equilibrium conditions like described in the literature.[30,50] For such a system having minimal strain, the electronic interactions are subtle, and no significant charge transfer is discerned between the layers.[30] Compared to this ideal vdW stacking, the interface between ML $MoS_2$ and $G_{bond}$ is different and exhibits a distinct interface coupling.

In principle, a reduction of the bandgap of ML $MoS_2/G_{bond}$ with respect to ML $MoS_2/G_{free}$ might be caused by unintended charge effects, strain effects, an interlayer mismatch, or a changed interlayer spacing.[29−31] However, the first reasons can be excluded, since both stackings, $MoS_2/G_{bond}$ and $MoS_2/G_{free}$, are nearly charge neutral (according to Raman measurements), almost strain-free, and exhibit a twist angle near 0°. Consequently, a difference in interlayer spacing is supposed to account for the observed bandgap reduction of 0.24 eV. According to theoretical studies, the increase of interactions between interfacial sulfur atoms ($MoS_2$) and SLG leads to a weakening of the intralayer Mo−S bonds and Mo d-states expanding into the bandgap at the CB edge.[24,31] In this connection, a reduction of the interface distance of about 10% is reported to cause a bandgap reduction of 10 to 80 meV at maximum.[30,31] This leads us to the suggestion that the here observed bandgap reduction of ML $MoS_2/G_{bond}$ with respect to ML $MoS_2/G_{free}$ is related to a larger reduction of the interface spacing, or other effects have to be considered as well. A further reason for the bandgap reduction might be the modification of the $\pi$-electron distribution of $G_{bond}$ with respect to $G_{free}$. The $p_z$-orbitals, located at the C atoms and forming the $\pi$-electron system of $G_{bond}$, are involved in weak hydrogen bonds to the top layer of the underlying $H_2$-etched sapphire and thus polarized (Figure 1b).[32] A polarized $G_{bond}$ is prone to provoke a charge redistribution at the $MoS_2/G_{bond}$ interface, which might weaken the intralayer Mo−S bonds additionally, so that the bandgap reduction is enhanced compared to a pure interlayer spacing effect. To elucidate this point, more detailed SPM measurements were performed.

The bandgap obtained from ML $MoS_2$ in contact with $G_{bond}/S$ was further investigated by atomic-scale STM and STS at different conditions allowing to discriminate between surface morphology and electronic effects. The STM images, Figure 5a,b, were measured on the identical position applying either a bias voltage inside or outside the bandgap (see also Supporting Information, Figure S5). Figure 5a reveals the surface layer sulfur atoms of the $MoS_2$ monolayer and additionally a moiré superstructure with the periodicity of 2.67 nm, which corresponds perfectly to the moiré superstructure of weakly bonded SLG on sapphire (Figure 5c).[32] Therefore, we assume that the defect-free ML $MoS_2$ conforms to the underlying SLG moiré superstructure with a reduced amplitude as indicated by a comparison of the height profiles in Figure 5e. While the SLG moiré structure usually exhibits apparent height differences of 40 pm (buckle−valley), the corrugation amplitude of the ML $MoS_2$ is around 10 pm. Some brighter buckles are randomly distributed, like the one shown in Figure 5a, having an apparent height of up to 16 pm. Provided that these height differences correspond predominantly to topographical differences, the $MoS_2$/SLG interlayer distance fluctuates periodically over the surface. Assuming a mean interlayer distance of 0.34 nm, the variation in the S···C distance from buckle to valley (30 pm) amounts up to 9%.

From STS curves performed on valleys and buckles (Figure 6a) of the $MoS_2/G_{bond}/S$ heterostructure, characteristic values for the conduction band minimum CBM(valley) = 164 ± 3 meV and CBM(buckle) = 153 ± 3 meV are obtained. Thus, we derive experimental evidence that a shorter $MoS_2$/SLG interlayer distance (at the side of the buckles) results in a shift of the CBM toward the Fermi level, while the valence band maximum stays almost constant (VBM(valley) = −1.840 ± 0.003 eV and VBM(buckle) = −1.841 ± 0.004 eV). Hence, the reduction of the interlayer distance (corresponding to an increase of the apparent height of the STS position) is proportional to the reduction of the $MoS_2$ bandgap (ΔBG) in the case of the buckle structure of $MoS_2/G_{bond}$ (Figure 6b). Based on the data given in Figures 5e and 6b, a slope of


https://doi.org/10.1021/acs.jpcc.3c02503
J. Phys. Chem. C 2023, 127, 10878−10887

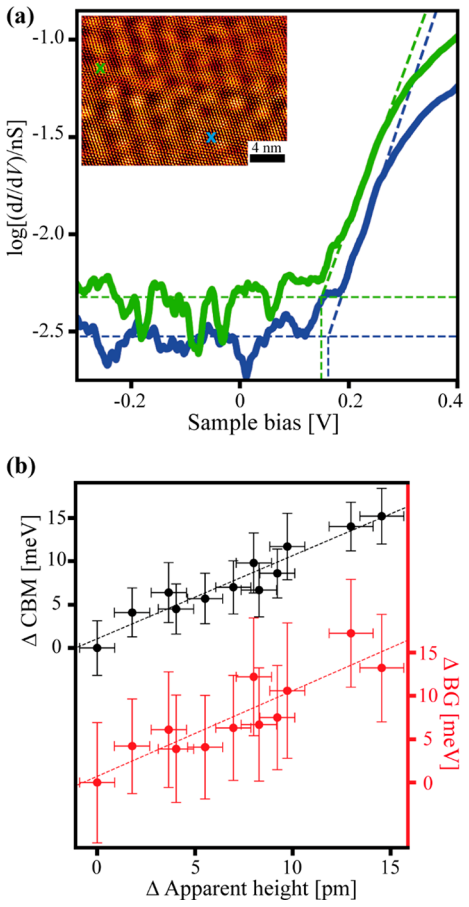


**Figure 6.** (a) Exemplary STS curves determined on a buckle (green) and a valley (blue) on the $MoS_2/G_{bond}/S$ heterostructure as indicated in the inset (STS: $I_{set}$ = 0.62 nA, $V_{bias}$ = 1.45 V; inset: $I_{set}$ = 3.1 nA, $V_{bias}$ = 0.41 V). The green curve is shifted upward by 0.3 for better visibility. (b) Shift of the CBM toward $E_F$ (ΔCBM = CBM(valley) − CBM(STS position), black curve) and reduction of the BG (ΔBG = BG(valley) − BG(STS position), red curve) with apparent height of the STS position (the averaged apparent heights of the valleys in the buckle structure of $MoS_2$ are defined as 0 pm).

ΔBG/Δinterlayer spacing of about 11 meV/30 pm can be estimated, which is in agreement with the lower theoretically deduced value.[31] That is, a variation of the interlayer spacing between ML $MoS_2$ and $G_{bond}$ causes only a minor reduction of the ML $MoS_2$ quasiparticle bandgap and can be ruled out as reason for the bandgap reduction of $MoS_2/G_{bond}$ compared to $MoS_2/G_{free}$ of 0.24 eV. Thus, this bandgap reduction is likely due to the modified $\pi$-electron distribution of $G_{bond}$ with respect to $G_{free}$ caused by the $G_{bond}/S$ interface interactions, as discussed above. This in turn will induce a further polarization of the interfacial Mo−S bonds and induce an interlayer dipole, even if no significant charge transfer is present between ML $MoS_2$ and $G_{bond}$.[24]

The electronic properties of the $MoS_2/G_{bond}/S$ heterostructure are further evaluated with STM imaging realized with $V_{bias}$ in the bandgap, like displayed in Figure 5b. Here, the same atomic structure as observed in Figure 5a is present, but the topographic buckle structure is overshadowed by seemingly random electronic structures. The brightest areas, corresponding to the highest electron densities, are often found at elevated positions on the heterostructure surface, like those marked by blue squares in Figure 5a,b. These bright areas verify the assumption that occasionally emerging high $MoS_2$ buckles are correlated to shorter S···C interface distances that enable a stronger interface coupling. In addition, there are hints from theoretical studies that local strain effects due to the larger curvature of ML $MoS_2$ may play a role at pronounced buckles as well.[30,31,57]

To further elucidate this point, the $MoS_2/G_{bond}/S$ heterostructure displaying surface areas with increased and decreased charge densities (Figure 7a) has been examined by

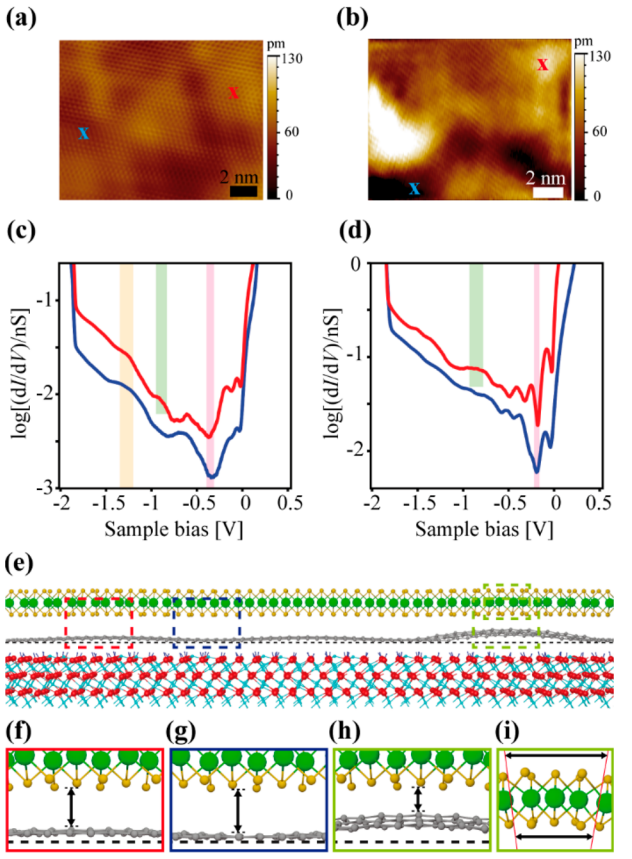


**Figure 7.** STM images of $MoS_2$ nanosheets on (a) $G_{bond}/S$ and (b) $G_{free}/S$ (measurement conditions in the bandgap $I_{set}$ = 0.5 nA, $V_{bias}$ = −0.3 V). (c) STS on $MoS_2/G_{bond}/S$ at the positions marked with a red and a blue cross in (a). (d) STS on $MoS_2/G_{free}/S$ at the positions marked with a red and a blue cross in (b). All STS measurements were taken at a tip position given by $I_{set}$ = 3.1 nA and $V_{bias}$ = 0.42 V. The red crosses and red curves correspond to bright areas in (a) and (b), while the blue crosses and curves correspond to dark areas. For the color code of bars in (c) and (d) see text. For reference STS on $G_{bond}/S$ and $G_{free}/S$, see Supporting Information, Figure S6. (e) Schematic showing the $MoS_2/G_{bond}/S$ heterostructure with 40 pm graphene buckles and one 160 nm graphene buckle. (f−h) Enlargement of the areas marked in (e) with a frame (amplification factor 5). (i) The schematic displays that bending of the ML $MoS_2$ causes increased (decreased) S···S distances at the outside (inside) sulfur layer (the $MoS_2$ curvature in this schematic is amplified by a factor of 20).

STS with a short tip−surface distance to record possible local in-gap electronic features.[32,34] Inspecting the STS curves obtained at random positions on the surface, we can clearly identify the Dirac point of SLG (marked with a red bar in Figure 7c) and a state which has been attributed to the $G_{bond}/S$ interface interactions previously (marked with an orange bar,


https://doi.org/10.1021/acs.jpcc.3c02503
J. Phys. Chem. C 2023, 127, 10878−10887

for details see Supporting Information, Figure S6).[32] Most interestingly, an additional in-gap state is recorded at −0.91 ± 0.05 V for $MoS_2/G_{bond}/S$ only on bright surface areas (Figure 7c, marked by a green bar). This local interface acceptor state shows a tendency to be located predominantly on top of pronounced buckles (Figure 7). This finding indicates that local bending strain effects, like observed for n-doped $MoS_2$ on a $SiO_2/Si$ surface with a considerably increased roughness compared to graphene,[56] have to be considered here as well. The existence of the additional in-gap state is also verified by a series of bias dependent STM images on the $MoS_2/G_{bond}/S$ heterostructure given in Supporting Information, Figure S5.

STS measurements performed on bright areas of the $MoS_2/G_{free}/S$ heterostructure (Figure 7b,d) also exhibit the in-gap state (−0.85 ± 0.05 V) that is attributed to local bending strain. As discussed above, the $MoS_2/G_{free}$ heterostructure exhibits only subtle electronic interface interactions. However, a certain roughness of the $G_{free}/S$ substrate due to sapphire step edges or graphene ripples is given, so that local bending strain affecting the $MoS_2$ ML may exist. Indeed, on bright areas of the $MoS_2/G_{free}/S$ heterostructure, the local $MoS_2$/SLG interface state is determined likewise. Altogether, it is correlated to exposed buckles on the SLG/S surface or other surface roughness but not sensitive to the small variations of the $MoS_2$/SLG interlayer distance.

Another obvious difference between the substrate regions $G_{bond}/S$ and $G_{free}/S$ is that the latter exhibits charge inhomogeneities, also described as electron and hole puddles, originating from $\pi-\pi$ orbital mixing due to the presence of ripples in free-standing SLG (Figure 7a,b).[32,58] Consequently, $MoS_2/G_{free}/S$ scanned with STM displays charge fluctuations caused by $G_{free}$ on all images. These electron and hole puddles can be observed best with $V_{bias}$ inside the $MoS_2$ bandgap due to the lack of $MoS_2$ states under these conditions (Supporting Information, Figure S7). The charge inhomogeneities in $MoS_2/G_{free}/S$ arising from $G_{free}$ have a considerably larger amplitude compared to the charge fluctuations located in the vdW gap between $MoS_2$ and $G_{bond}$ in the $MoS_2/G_{bond}/S$ heterostructure, as can be directly recognized from Figure 7a,b plotted in the same color scale. This suggests a rather small charge density in the vdW gap between $MoS_2$ and $G_{bond}$ arising from interface coupling.

Another point worth to consider is the shift of the SLG Dirac point due to the approach of the STM tip. In the heterostructure $MoS_2/G_{free}/S$, we observe a shift to −0.19 V, comparable to the one measured for $G_{free}/S$ previously.[32,59] This observation confirms the view that almost free-standing SLG forms no relevant contact to the underlying sapphire and $MoS_2/G_{free}$ can be regarded as an almost free-standing heterostructure with only minor interface coupling exhibiting no charge redistribution.[30] In contrast, the heterostructure $MoS_2/G_{bond}/S$ exhibits a shift of the Dirac point to −0.35 V. However, this shift is in line with the shift of the CBM toward $E_F$ present only in $MoS_2/G_{bond}/S$. Consequently, we attribute the Dirac point shift, in analogy to theory,[31] to the charge redistribution at the $MoS_2/G_{bond}$ interface that leads to the formation of an interface dipole. This dipole causes a band realignment at the $MoS_2/G_{bond}$ interface, which we observe as downward shift of the Dirac point.

These results reveal the distinct influence of the SLG coupling strength to the underlying $\alpha$-$Al_2O_3$ (0001) on the electronic properties of the $MoS_2$/SLG/S heterostructure. We are convinced that differences observed in the $MoS_2$/graphene interlayer coupling, leading for example to varying bandgap values, can be explained, if the impact of the underlying substrate is respected in detail. Regarding device performance in general, besides the known direct influences on the $MoS_2$/SLG heterostructure, also effects influencing the SLG/S substrate should be considered. Impacts, like aging, intercalation, or thermal effects, will affect the SLG/S interface coupling and, thus, have an indirect influence on the electronic structure of $MoS_2$/SLG/S devices.

## 4. CONCLUSION

In summary, we employed vdW epitaxy using a MOVPE process to deposit ML and BL 2H-$MoS_2$ nanosheets in registry on an SLG/S substrate exhibiting two distinctly different substrate regions, $G_{bond}/S$ and $G_{free}/S$. The resulting $MoS_2/G_{free}/S$ stacking is composed of free-standing, charge neutral, and almost strain-free $MoS_2$ and graphene with only subtle interface interactions. Compared to this prototypical vdW heterostructure used as an internal reference, the increased coupling strength of ML $MoS_2$ toward $G_{bond}/S$ was clearly identified, which leads to a shift of the CB edge and a bandgap reduction of 0.24 eV. ML $MoS_2$ nanosheets deposited on $G_{bond}/S$ follow the buckle structure of $G_{bond}$ with reduced amplitude. Employing STS on the buckled ML $MoS_2/G_{bond}/S$ heterostructure, we have shown that variations in the interface spacing between ML $MoS_2$ and SLG have only a minor effect on the $MoS_2$ bandgap. In addition, an in-gap acceptor state was identified, which was attributed to local bending strain present in ML $MoS_2$ provoked by the local roughness of the SLG/S substrate. These findings indicate that the interface coupling of graphene and sapphire affects the electronic structure of the $MoS_2$/SLG heterostructure and, thus, substrate aging effects might also influence the electronic properties of $MoS_2$/SLG/S based devices.

## ■ ASSOCIATED CONTENT

### Supporting Information

The Supporting Information is available free of charge at https://pubs.acs.org/doi/10.1021/acs.jpcc.3c02503.

Additional experimental details as well as Raman, AFM, STM, and STS data (PDF)

## ■ AUTHOR INFORMATION


### Corresponding Authors

**Susanne Hoffmann-Eifert** − *JARA-Institute Energy-efficient Information Technology (Green IT & PGI-10), Forschungszentrum Jülich GmbH, 52425 Jülich, Germany;* orcid.org/0000-0003-1682-826X; Email: su.hoffmann@fz-juelich.de

**Silvia Karthäuser** − *Peter Grünberg Institut 7, Forschungszentrum Jülich GmbH and JARA-FIT, 52425 Jülich, Germany;* orcid.org/0000-0003-3953-6980; Email: s.karthaeuser@fz-juelich.de

### Authors

**Henrik Wördenweber** − *Peter Grünberg Institut 7, Forschungszentrum Jülich GmbH and JARA-FIT, 52425 Jülich, Germany; RWTH Aachen University, 52056 Aachen, Germany*

**Annika Grundmann** − *Compound Semiconductor Technology, RWTH Aachen University, 52074 Aachen, Germany*

**Zhaodong Wang** − *Peter Grünberg Institut 7, Forschungszentrum Jülich GmbH and JARA-FIT, 52425 Jülich, Germany; JARA-Institute Energy-efficient Information Technology (Green IT & PGI-10), Forschungszentrum Jülich GmbH, 52425 Jülich, Germany*

**Holger Kalisch** − *Compound Semiconductor Technology, RWTH Aachen University, 52074 Aachen, Germany*

**Andrei Vescan** − *Compound Semiconductor Technology, RWTH Aachen University, 52074 Aachen, Germany;* orcid.org/0000-0001-9465-2621

**Michael Heuken** − *Compound Semiconductor Technology, RWTH Aachen University, 52074 Aachen, Germany; AIXTRON SE, 52134 Herzogenrath, Germany*

**Rainer Waser** − *Peter Grünberg Institut 7, Forschungszentrum Jülich GmbH and JARA-FIT, 52425 Jülich, Germany; JARA-Institute Energy-efficient Information Technology (Green IT & PGI-10), Forschungszentrum Jülich GmbH, 52425 Jülich, Germany; Institute of Materials in Electrical Engineering and Information Technology II, RWTH Aachen University, 52074 Aachen, Germany*

Complete contact information is available at: https://pubs.acs.org/10.1021/acs.jpcc.3c02503

### Author Contributions

S.H. planned the experiments. Z.W., A.G., and M.H. provided the sample. H.W. performed the SEM, Raman, AFM, LT-UHV-STM, and STS measurements and analyzed all data. H.W. and S.K. wrote the manuscript with contributions of all authors. S.K. and S.H. supervised the study. All authors have given approval to the final version of the manuscript.

### Notes

The authors declare no competing financial interest.

## ■ ACKNOWLEDGMENTS

This work was in parts funded by the Federal Ministry of Education and Research (BMBF, Germany) in the projects NEUROTEC (Project Nos. 16ME0398K, 16ME0399, and 16ME0403) and NeuroSys (Project Nos. 03ZU1106AA, 03ZU1106AB) and it is based on the Jülich Aachen Research Alliance (JARA-FIT).

## ■ REFERENCES

(1) Duong, D. L.; Yun, S. J.; Lee, Y. H. Van der Waals layered materials: Opportunities and challenges. *ACS Nano* **2017**, *11*, 11803−11830.

(2) Wang, Q. H.; Kalantar-Zadeh, K.; Kis, A.; Coleman, J. N.; Strano, M. S. Electronics and optoelectronics of two-dimensional transition metal dichalcogenides. *Nat. Nanotechnol.* **2012**, *7*, 699−712.

(3) Castellanos-Gomez, A. Why all the fuss about 2D semiconductors? *Nat. Photonics* **2016**, *10*, 202−204.

(4) Rasmussen, F. A.; Thygesen, K. S. Computational 2D materials database: Electronic structure of transition-metal dichalcogenides and oxides. *J. Phys. Chem. C* **2015**, *119*, 13169−13183.

(5) Splendiani, A.; Sun, L.; Zhang, Y.; Li, T.; Kim, J.; Chim, C. Y.; Galli, G.; Wang, F. Emerging photoluminescence in monolayer $MoS_2$. *Nano Lett.* **2010**, *10*, 1271−1275.

(6) Mak, K. F.; Lee, C.; Hone, J.; Shan, J.; Heinz, T. F. Atomically thin $MoS_2$: A new direct-gap semiconductor. *Phys. Rev. Lett.* **2010**, *105*, 136805.

(7) Ryou, J.; Kim, Y. S.; KC, S.; Cho, K. Monolayer $MoS_2$ bandgap modulation by dielectric environments and tunable bandgap transistors. *Sci. Rep.* **2016**, *6*, 29184.

(8) Mak, K. F.; He, K.; Lee, C.; Lee, G. H.; Hone, J.; Heinz, T. F.; Shan, J. Tightly bound trions in monolayer $MoS_2$. *Nat. Mater.* **2013**, *12*, 207−211.

(9) Novoselov, K.; Geim, A.; Morozov, S.; Jiang, D.; Katsnelson, M.; Grigorieva, I.; Dubonos, S.; Firsov, A. Two-dimensional gas of massless Dirac fermions in graphene. *Nature* **2005**, *438*, 197−200.

(10) Lee, C.; Rathi, S.; Khan, M. A.; Lim, D.; Kim, Y.; Yun, S. J.; Youn, D. H.; Watanabe, K.; Taniguchi, T.; Kim, G. H. Comparison of trapped charges and hysteresis behavior in hBN encapsulated single $MoS_2$ flake based field effect transistors on $SiO_2$ and hBN substrates. *Nanotechnology* **2018**, *29*, 335202.

(11) Mukherjee, S.; Maiti, R.; Midya, A.; Das, S.; Ray, S. K. Tunable direct bandgap optical transitions in $MoS_2$ nanocrystals for photonic devices. *ACS Photon.* **2015**, *2*, 760−768.

(12) McDonnell, S. J.; Wallace, R. M. Atomically-thin layered films for device applications based upon 2D TMDC materials. *Thin Solid Films* **2016**, *616*, 482−501.

(13) Farronato, M.; Melegari, M.; Ricci, S.; Hashemkhani, S.; Bricalli, A.; Ielmini, D. Memtransistor devices based on $MoS_2$ multilayers with volatile switching due to Ag cation migration. *Adv. Electron. Mater.* **2022**, *8*, 2101161.

(14) Li, X.; Zhu, H. Two-dimensional $MoS_2$: Properties, preparation, and applications. *J. Materiomics* **2015**, *1*, 33−44.

(15) Yu, L.; Lee, Y. H.; Ling, X.; Santos, E. J. G.; Shin, Y. C.; Lin, Y.; Dubey, M.; Kaxiras, E.; Kong, J.; Wang, H.; et al. Graphene/$MoS_2$ hybrid technology for large-scale two-dimensional electronics. *Nano Lett.* **2014**, *14*, 3055−3063.

(16) Roy, K.; Padmanabhan, M.; Goswami, S.; Sai, T. P.; Ramalingam, G.; Raghavan, S.; Ghosh, A. Graphene-$MoS_2$ hybrid structures for multifunctional photoresponsive memory devices. *Nat. Nanotechnol.* **2013**, *8*, 826−830.

(17) Liu, X.; Balla, I.; Bergeron, H.; Campbell, G. P.; Bedzyk, M. J.; Hersam, M. C. Rotationally commensurate growth of $MoS_2$ on epitaxial graphene. *ACS Nano* **2016**, *10*, 1067−1075.

(18) Hall, J.; Pielic, B.; Murray, C.; Jolie, W.; Wekking, T.; Busse, C.; Kralj, M.; Michely, T. Molecular beam epitaxy of quasi-freestanding transition metal disulphide monolayers on van der Waals substrates: A growth study. *2D Materials* **2018**, *5*, 025005.

(19) Kim, Y.; Choi, D.; Woo, W. J.; Lee, J. B.; Ryu, G. H.; Lim, J. H.; Lee, S.; Lee, Z.; Im, S.; Ahn, J. H.; et al. Synthesis of two-dimensional $MoS_2$/graphene heterostructure by atomic layer deposition using $MoF_6$ precursor. *Appl. Surf. Sci.* **2019**, *494*, 591−599.

(20) Hoang, A. T.; Katiyar, A. K.; Shin, H.; Mishra, N.; Forti, S.; Coletti, C.; Ahn, J. H. Epitaxial growth of wafer-scale molybdenum disulfide/graphene heterostructures by metal-organic vapor-phase epitaxy and their application in photodetectors. *ACS Appl. Mater. & Interfaces* **2020**, *12*, 44335−44344.

(21) Schneider, D. S.; Grundmann, A.; Bablich, A.; Passi, V.; Kataria, S.; Kalisch, H.; Heuken, M.; Vescan, A.; Neumaier, D.; Lemme, M. C. Highly responsive flexible photodetectors based on MOVPE grown uniform few-layer $MoS_2$. *ACS Photonics* **2020**, *7*, 1388−1395.

(22) Grundmann, A.; McAleese, C.; Conran, B. R.; Pakes, A.; Andrzejewski, D.; Kümmell, T.; Bacher, G.; Teo, K. B. K.; Heuken, M.; Kalisch, H.; et al. MOVPE of large-scale $MoS_2$/$WS_2$, $WS_2$/$MoS_2$, $WS_2$/graphene and $MoS_2$/graphene 2D-2D heterostructures for optoelectronic applications. *MRS Adv.* **2020**, *5*, 1625−1633.

(23) Cheng, Z.; Zhang, H.; Le, S. T.; Abuzaid, H.; Li, G.; Cao, L.; Davydov, A.; Franklin, A. D.; Richter, C. A. Are 2D interfaces really flat? *ACS Nano* **2022**, *16*, 5316−5324.

(24) Gong, C.; Colombo, L.; Wallace, R. M.; Cho, K. The unusual mechanism of partial Fermi level pinning at metal-$MoS_2$ interfaces. *Nano Lett.* **2014**, *14*, 1714−1720.

(25) Huang, Y. L.; Chen, Y.; Zhang, W.; Quek, S. Y.; Chen, C.-H.; Li, L.-J.; Hsu, W.-T.; Chang, W.-H.; Zheng, Y. J.; Chen, W.; et al. Bandgap tunability at single-layer molybdenum disulphide grain boundaries. *Nat. Commun.* **2015**, *6*, 6298.

(26) Trainer, D. J.; Zhang, Y.; Bobba, F.; Xi, X.; Hla, S.-W.; Iavarone, M. The effects of atomic-scale strain relaxation on the electronic properties of monolayer $MoS_2$. *ACS Nano* **2019**, *13*, 8284−8291.

(27) Zhang, C.; Johnson, A.; Hsu, C. L.; Li, L. J.; Shih, C. K. Direct imaging of band profile in single layer $MoS_2$ on graphite: Quasiparticle energy gap, metallic edge states, and edge band bending. *Nano Lett.* **2014**, *14*, 2443−2447.
(28) Trainer, D. J.; Putilov, A. V.; Di Giorgio, C.; Saari, T.; Wang, B.; Wolak, M.; Chandrasena, R. U.; Lane, C.; Chang, T.-R.; Jeng, H.-T.; et al. Inter-Layer Coupling Induced Valence Band Edge Shift in Mono- to Few-Layer $MoS_2$. *Sci. Rep.* **2017**, *7*, 40559.
(29) Ebnonnasir, A.; Narayanan, B.; Kodambaka, S.; Ciobanu, C. V. Tunable $MoS_2$ bandgap in $MoS_2$-graphene heterostructures. *Appl. Phys. Lett.* **2014**, *105*, 031603.
(30) Singh, S.; Espejo, C.; Romero, A. H. Structural, electronic, vibrational, and elastic properties of graphene/$MoS_2$ bilayer heterostructures. *Phys. Rev. B* **2018**, *98*, 155309.
(31) Fang, Q.; Li, M.; Zhao, X.; Yuan, L.; Wang, B.; Xia, C.; Ma, F. Van der Waals graphene/$MoS_2$ heterostructures: Tuning the electronic properties and Schottky barrier by applying a biaxial strain. *Mater. Adv.* **2022**, *3*, 624−631.
(32) Wördenweber, H.; Karthäuser, S.; Grundmann, A.; Wang, Z.; Aussen, S.; Kalisch, H.; Vescan, A.; Heuken, M.; Waser, R.; Hoffmann-Eifert, S. Atomically resolved electronic properties in single layer graphene on $\alpha$-$Al_2O_3$ (0001) by chemical vapor deposition. *Sci. Rep.* **2022**, *12*, 18743.
(33) Peng, W.; Wang, H.; Lu, H.; Yin, L.; Wang, Y.; Grandidier, B.; Yang, D.; Pi, X. Recent progress on the scanning tunneling microscopy and spectroscopy study of semiconductor heterojunctions. *Small* **2021**, *17*, 2100655.
(34) Schmidt, N.; Rushchanskii, K. Z.; Trstenjak, U.; Dittmann, R.; Karthäuser, S. In-gap states of $HfO_2$ nanoislands driven by crystal nucleation: Implications for resistive random-access memory devices. *ACS Appl. Nano Mater.* **2023**, *6*, 148−159.
(35) Glöss, M.; Pütt, R.; Moors, M.; Kentzinger, E.; Karthäuser, S.; Monakhov, K. Y. Exploring the ligand functionality, electronic band gaps, and switching characteristics of single Wells-Dawson-type polyoxometalates on gold. *Adv. Mater. Interfaces* **2022**, *9*, 2200461.
(36) Zhou, K.-G.; Withers, F.; Cao, Y.; Hu, S.; Yu, G.; Casiraghi, C. Raman modes of $MoS_2$ used as fingerprint of van der Waals interactions in 2-D crystal-based heterostructures. *ACS Nano* **2014**, *8*, 9914−9924.
(37) Hui, Y. Y.; Liu, X.; Jie, W.; Chan, N. Y.; Hao, J.; Hsu, Y.-T.; Li, L.-J.; Guo, W.; Lau, S. P. Exceptional tunability of band energy in a compressively strained trilayer $MoS_2$ sheet. *ACS Nano* **2013**, *7*, 7126−7131.
(38) Zhang, X.; Yang, H.; Hou, W.; Zheng, X.; Zhang, Y.; Zhang, R.; Deng, C.; Zhang, X.; Qin, S. Twist-angle modulation of exciton absorption in $MoS_2$/graphene heterojunctions. *Appl. Phys. Lett.* **2019**, *115*, 181901.
(39) Chakraborty, B.; Bera, A.; Muthu, D. V. S.; Bhowmick, S.; Waghmare, U. V.; Sood, A. K. Symmetry-dependent phonon renormalization in monolayer $MoS_2$ transistor. *Phys. Rev. B* **2012**, *85*, 161403.
(40) Buscema, M.; Steele, G. A.; van der Zant, H. S. J.; Castellanos-Gomez, A. The effect of the substrate on the Raman and photoluminescence emission of single-layer $MoS_2$. *Nano Res.* **2014**, *7*, 561−571.
(41) Rice, C.; Young, R. J.; Zan, R.; Bangert, U.; Wolverson, D.; Georgiou, T.; Jalil, R.; Novoselov, K. S. Raman-scattering measurements and first-principles calculations of strain-induced phonon shifts in monolayer $MoS_2$. *Phys. Rev. B* **2013**, *87*, 081307.
(42) McCreary, K. M.; Hanbicki, A. T.; Robinson, J. T.; Cobas, E.; Culbertson, J. C.; Friedman, A. L.; Jernigan, G. G.; Jonker, B. Large-area synthesis of continuous and uniform $MoS_2$ monolayer films on graphene. *Adv. Funct. Mater.* **2014**, *24*, 6449−6454.
(43) Berciaud, S.; Ryu, S.; Brus, L. E.; Heinz, T. F. Probing the intrinsic properties of exfoliated graphene: Raman spectroscopy of free-standing monolayers. *Nano Lett.* **2009**, *9*, 346−352.
(44) Stampfer, C.; Molitor, F.; Graf, D.; Ensslin, K.; Jungen, A.; Hierold, C.; Wirtz, L. Raman imaging of doping domains in graphene on $SiO_2$. *Appl. Phys. Lett.* **2007**, *91*, 241907.
(45) Tsoukleri, G.; Parthenios, J.; Papagelis, K.; Jalil, R.; Ferrari, A. C.; Geim, A. K.; Novoselov, K. S.; Galiotis, C. Subjecting a graphene monolayer to tension and compression. *Small* **2009**, *5*, 2397−2402.
(46) Lee, J. E.; Ahn, G.; Shim, J.; Lee, Y. S.; Ryu, S. Optical separation of mechanical strain from charge doping in graphene. *Nat. Commun.* **2012**, *3*, 1024.
(47) Neumann, C.; Reichardt, S.; Venezuela, P.; Droegeler, M.; Banszerus, L.; Schmitz, M.; Watanabe, K.; Taniguchi, T.; Mauri, F.; Beschoten, B.; et al. Raman spectroscopy as probe of nanometre-scale strain variations in graphene. *Nat. Commun.* **2015**, *6*, 8429.
(48) Yang, M.; Wang, L.; Hu, G.; Chen, X.; Gong, P. L.; Cong, X.; Liu, Y.; Yang, Y.; Li, X.; Zhao, X.; et al. Optical identification of interlayer coupling of graphene/$MoS_2$ van der Waals heterostructures. *Nano Res.* **2021**, *14*, 2241−2246.
(49) Faugeras, C.; Berciaud, S.; Leszczynski, P.; Henni, Y.; Nogajewski, K.; Orlita, M.; Taniguchi, T.; Watanabe, K.; Forsythe, C.; Kim, P.; et al. Landau level spectroscopy of electron-electron interactions in graphene. *Phys. Rev. Lett.* **2015**, *114*, 126804.
(50) Pierucci, D.; Henck, H.; Avila, J.; Balan, A.; Naylor, C. H.; Patriarche, G.; Dappe, Y. J.; Silly, M. G.; Sirotti, F.; Johnson, A. T. C.; et al. Band alignment and minigaps in monolayer $MoS_2$-graphene van der Waals Heterostructures. *Nano Lett.* **2016**, *16*, 4054−4061.
(51) Bronsema, K. D.; de Boer, J. L.; Jellinek, F. On the structure of molybdenum diselenide and disulfide. *Z. Anorg. Allg. Chem.* **1986**, *540*, 15−17.
(52) Hus, S. M.; Ge, R.; Chen, P. A.; Liang, L.; Donnelly, G. E.; Ko, W.; Huang, F.; Chiang, M. H.; Li, A. P.; Akinwande, D. Observation of single-defect memristor in an $MoS_2$ atomic sheet. *Nat. Nanotechnol.* **2021**, *16*, 58−62.
(53) Shi, H.; Pan, H.; Zhang, Y. W.; Yakobson, B. I. Quasiparticle band structures and optical properties of strained monolayer $MoS_2$ and $WS_2$. *Phys. Rev. B* **2013**, *87*, 155304.
(54) Vancso, P.; Magda, G. Z.; Peto, J.; Noh, J. Y.; Kim, Y. S.; Hwang, C.; Biro, L. P.; Tapaszto, L. The intrinsic defect structure of exfoliated $MoS_2$ single layers revealed by scanning tunneling microscopy. *Sci. Rep.* **2016**, *6*, 29726.
(55) Chen, F. X. R.; Kawakami, N.; Lee, C. T.; Shih, P. Y.; Wu, Z. C.; Yang, Y. C.; Tu, H. W.; Jian, W. B.; Hu, C.; Lin, C. L. Visualizing correlation between carrier mobility and defect density in $MoS_2$ FET. *Appl. Phys. Lett.* **2022**, *121*, 151601.
(56) Ugeda, M. M.; Bradley, A. J.; Shi, S. F.; da Jornada, F. H.; Zhang, Y.; Qiu, D. Y.; Ruan, W.; Mo, S. K.; Hussain, Z.; Shen, Z. X.; et al. Giant bandgap renormalization and excitonic effects in a monolayer transition metal dichalcogenide semiconductor. *Nat. Mater.* **2014**, *13*, 1091−1095.
(57) Shin, B. G.; Han, G. H.; Yun, S. J.; Oh, H. M.; Bae, J. J.; Song, Y. J.; Park, C. Y.; Lee, Y. H. Indirect bandgap puddles in monolayer $MoS_2$ by substrate-induced local strain. *Adv. Mater.* **2016**, *28*, 9378−9384.
(58) Xue, J.; Sanchez-Yamagishi, J.; Bulmash, D.; Jacquod, P.; Deshpande, A.; Watanabe, K.; Taniguchi, T.; Jarillo-Herrero, P.; LeRoy, B. J. Scanning tunneling microscopy and spectroscopy of ultra-flat graphene on hexagonal boron nitride. *Nat. Mater.* **2011**, *10*, 282−285.
(59) Kobayashi, K.; Isshiki, N.; Tsukada, M. Effect of tip atomic-structure on scanning tunneling spectroscopy. *Solid State Commun.* **1990**, *74*, 1187−1191.


https://doi.org/10.1021/acs.jpcc.3c02503
J. Phys. Chem. C 2023, 127, 10878−10887